Robust Control Design for Active Flutter Suppression

Julian Theis*, Harald Pfifer† and Peter Seiler‡
University of Minnesota, Minneapolis, MN 55455, USA

Flutter is an unstable oscillation caused by the interaction of aerodynamics and structural dynamics. It can lead to catastrophic failure and therefore must be strictly avoided. Weight reduction and aerodynamically efficient high aspect ratio wing design reduce structural stiffness and thus reduce flutter speed. Consequently, the use of active control systems to counter these adverse aeroservoelastic effects becomes an increasingly important aspect for future flight control systems. The paper describes the process of designing a controller for active flutter suppression on a small, flexible unmanned aircraft. It starts from a grey-box model and highlights the importance of individual components such as actuators and computation devices. A systematic design procedure for an $\mathcal{H}_\infty$-norm optimal controller that increases structural damping and suppresses flutter is then developed. A second key contribution is the development of thorough robustness tests for clearance in the absence of a high-fidelity nonlinear model.

I. Introduction

Aeroelastic flutter involves the adverse interaction of aerodynamics with structural dynamics and produces an unstable oscillation that often results in structural failure. Conventional aircraft are designed such that flutter does not occur within their range of operating conditions. This is usually achieved through the use of stiffening materials and thus at the expense of additional structural mass. The use of active control systems to expand the flutter boundary could therefore lead to a decrease in structural mass and consequently increase fuel efficiency and performance for future aircraft. The present paper contributes a systematic $\mathcal{H}_\infty$ control design for the University of Minnesota's mini MUTT (Multi Utility Technology Testbed) aircraft. The mini MUTT is a small, remote-piloted aircraft that resembles Lockheed Martin's Body Freedom Flutter vehicle[1] and NASA's X56 MUTT aircraft.[2]

Early research on active flutter suppression relied to a large extend on what is known as *collocated feedback* within the structural control community. Collocated feedback employs sensors and actuators in the same location. The special property of such feedback loops is the presence of a complex pair of zeros in the immediate vicinity of the lightly damped poles of the structural mode, see e. g. Ref. 3. A closely related approach, termed the concept of *identically located force and acceleration* in Ref. 4, was successfully applied to address the damping of structural modes on the B-1 aircraft.[5,6] A similar configuration was also used in the first flight test beyond flutter speed, conducted in 1973 on a modified B-52 aircraft.[7] The control system on that aircraft involved two single feedback loops that fed back filtered vertical acceleration signals, acquired on the wing, to control surfaces located nearby (outboard ailerons and flaperons). Collocated acceleration feedback is also proposed in various other publications concerned with flutter suppression, e. g. Refs. 8–11. Collocated controllers are, in general, easily designed using root-locus analysis and have favorable robustness properties. For the mini MUTT aircraft, however, collocated acceleration feedback tends to destabilize the short period dynamics. This is attributed to two facts. First, the collocated control surfaces (outboard flaps) have a much higher pitch effectiveness on a flying-wing compared to ailerons on a conventional aircraft. Second, the frequencies of the short period dynamics and the aeroelastic modes are very close to each other, making a frequency separation difficult to achieve. An alternative design approach for a flutter suppression controller is therefore required.

*Research Fellow, Aerospace Engineering and Mechanics Department, email: theis476@umn.edu
†Post-Doctoral Associate, Aerospace Engineering and Mechanics Department, email: hpfifer@umn.edu
‡Assistant Professor, Aerospace Engineering and Mechanics Department, email: seile017@umn.edu

A recent flight test demonstration of active flutter suppression on Lockheed Martin's Body Freedom Flutter vehicle is reported in Ref 12. A blend of multivariable linear quadratic Gaussian (LQG) controllers is used, but due to the proprietary nature of the research, little detail about the design is provided. NASA Dryden is also currently developing multivariable flutter suppression controllers based on LQG techniques for their X-56 MUTT aircraft, see Ref. 2. An $\mathcal{H}_\infty$ control design for the X-56 is detailed in Ref. 13 and also extended to linear parameter-varying (LPV) control. Similar multivariable robust control designs for flutter suppression were previously reported in References 14–16.

For the present paper, $\mathcal{H}_\infty$ closed-loop shaping is selected as the control design method. It is believed to be particularly suitable for the considered application for three main reasons. First, the objective of providing damping is easy to express in terms of reducing peaks in the frequency response of closed-loop transfer functions. Second, control activity is easy to confine to a specific frequency range. Roll-off and wash-out filters can be directly incorporated into the controller, without the need of ad-hoc modifications. This avoids undesired interaction of the control loop with unmodeled parts of the plant or different layers of control systems. Finally, $\mathcal{H}_\infty$ controllers minimize a worst-case metric. They thus tend to provide a high level of inherent robustness when all possible loop break points are included in the performance specifications. The latter two reasons are considered advantages over other popular multivariable design techniques such as LQG control.

A mathematical model of the mini MUTT aircraft is described in Section II, with an emphasis on accurately capturing phase loss due to parasitic dynamics. Section III provides the necessary background about $\mathcal{H}_\infty$ control and details the design of an active flutter suppression controller with a mixed sensitivity formulation. The controller is analyzed with respect to a variety of stability margins in Section IV and shown to be very robust. The design presented in this paper parallels ongoing research on flutter suppression for the mini MUTT vehicle based on an adaptive linear quadratic regulator formulation (Ref. 17) and on pitch rate feedback (Ref. 18). Flight tests are scheduled for spring 2016 and will provide a comparison of the different approaches.

II. Modeling of the Aircraft

The aircraft under consideration in this paper is the mini MUTT, built at the University of Minnesota, Minneapolis. It is a remote-piloted flying wing aircraft with a wing span of 3 m and a total mass of about 6.7 kg. The design closely resembles Lockheed Martin's Body Freedom Flutter vehicle[1] and NASA's X56 MUTT aircraft.[2] The mini MUTT is designed such that it exhibits strong coupling of rigid body dynamics and structural dynamics at low airspeeds. Flutter occurs above an airspeed of 30 m/s. Without active flutter suppression, the inevitable result is catastrophic structural failure as shown in the picture sequence in Figures 1a–e.

(a) (b) (c) (d) (e)

Figure 1. Open-loop flutter and catastrophic failure during a flight test slightly above 30 m/s indicated airspeed at the University of Minnesota on August 25th 2015.

A. Grey-Box Identification and Synthesis Model

The modeling procedure is described in detail in Refs. 19,20. The model is based on a mean-axis description[21] and considers only longitudinal dynamics for straight and level flight under small elastic deformations. The state space representation contains four states associated with rigid body dynamics, namely the forward velocity u, angle of attack α, pitch angle θ, and pitch rate q. Additionally, the first three symmetric free vibration modes are included in the model. The modes are described by their generalized displacements $\{\eta_i\}_{i=1}^{3}$

and velocities $\{\dot{\eta}_i\}_{i=1}^{3}$. With the state vector $x = [u \;\; \alpha \;\; \theta \;\; q \;\; \eta_1 \;\; \dot{\eta}_1 \;\; \eta_2 \;\; \dot{\eta}_2 \;\; \eta_3 \;\; \dot{\eta}_3]^T$, the state equation is

$$\dot{x} = \begin{bmatrix} X_u & X_\alpha & -g & X_q & 0 & 0 & \cdots & 0 & 0 \\ Z_u/V & Z_\alpha/V & 0 & 1+Z_q/V & Z_{\eta_1}/V & Z_{\dot{\eta}_1}/V & \cdots & Z_{\eta_3}/V & Z_{\dot{\eta}_3}/V \\ 0 & 0 & 0 & 1 & 0 & 0 & \cdots & 0 & 0 \\ M_u & M_\alpha & 0 & M_q & M_{\eta_1} & M_{\dot{\eta}_1} & \cdots & M_{\eta_3} & M_{\dot{\eta}_3} \\ 0 & 0 & 0 & 0 & 0 & 1 & \cdots & 0 & 0 \\ 0 & \Xi_{1}\alpha & 0 & \Xi_{1}q & \Xi_{1\eta_1}-\omega_1^2 & \Xi_{1\dot{\eta}_1}-2\omega_1\zeta_1 & \cdots & \Xi_{1\eta_3} & \Xi_{1\dot{\eta}_3} \\ \vdots & \vdots & \vdots & \vdots & \vdots & \vdots & & \vdots & \vdots \\ 0 & 0 & 0 & 0 & 0 & 1 & \cdots & 0 & 0 \\ 0 & \Xi_{3}\alpha & 0 & \Xi_{3}q & \Xi_{3\eta_1} & \Xi_{3\dot{\eta}_1} & \cdots & \Xi_{3\eta_3}-\omega_3^2 & \Xi_{3\dot{\eta}_3}-2\omega_3\zeta_3 \end{bmatrix} x + \begin{bmatrix} X_{\delta_1} & X_{\delta_2} \\ Z_{\delta_1}/V & Z_{\delta_2}/V \\ 0 & 0 \\ M_{\delta_1} & M_{\delta_2} \\ 0 & 0 \\ \Xi_{1\delta_1} & \Xi_{1\delta_2} \\ \vdots & \vdots \\ 0 & 0 \\ \Xi_{3\delta_1} & \Xi_{3\delta_2} \end{bmatrix} \delta. \tag{1}$$

The plant input $\delta = [\delta_1 \;\; \delta_2]^T$ consists of symmetric midboard flap deflection δ_1 and symmetric outboard flap deflection δ_2. The entries X_i, Z_i, M_i and $\Xi_{k,i}$ for $i \in \{u, \alpha, q, \eta_1, \dot{\eta}_1, \eta_3, \dot{\eta}_3, \delta_1, \delta_2\}$ and $k = 1, 2, 3$ are dimensional aerodynamic derivatives. The entries ω_k and ζ_k are the eigenfrequencies and damping ratios of the k^{th} structural mode and g denotes the gravitational acceleration. The values of the aerodynamic coefficients are initially computed by a vortex lattice method.[20] Flight data, obtained in system identification flights at 23 m/s, were used to update the coefficients Z_i, M_i, $\Xi_{1,i}$ for $i \in \{\alpha, q, \eta_1, \dot{\eta}_1, \delta_1, \delta_2\}$ in Ref. 19. These coefficients are associated with the short period dynamics and the first flexible mode. An output equation $y = C\,x + D\,\delta$ can be added to Eq. (1) using the mode shapes of the structural modes. For further details, the reader is referred to Refs. 19, 20 and references therein.

For the flutter suppression control design, the pitch rate and the vertical acceleration at both the center of gravity and at the wing tips are used, i. e., $y = [q \;\; a_{z,\text{CG}} \;\; a_{z,\text{WT}}]^T$. The controller is assigned full authority over the outboard flaps, i. e., $\delta_2 = u$. The midboard flaps remain reserved for exclusive use by the pilot. Keeping the flutter suppression control loop completely separate from pilot inputs reduces the risk of saturating the control surfaces and facilitates a simple control design. A schematic showing the aircraft with the sensor and actuator positions is depicted in Figure 2. In order to simplify the synthesis model, the states u and θ are removed by truncation and the states $\eta_2, \dot{\eta}_2, \eta_3, \dot{\eta}_3$ are residualized. The resulting model thus only consists of four states, $\alpha, q, \eta_1, \dot{\eta}_1$, and can be interpreted as a short period approximation that includes the first aeroelastic mode. Both the short period and aeroelastic mode contain contributions from all four states, which shows that there is no clear separation between rigid body and structural dynamics. The short period frequency is around 25 rad/s with a damping ratio 0.8 for a flight speed of 30 m/s. The aeroelastic mode at that airspeed has a frequency of 33 rad/s and is marginally stable. This agrees well with the observed flutter speed of slightly above 30 m/s in flight tests.

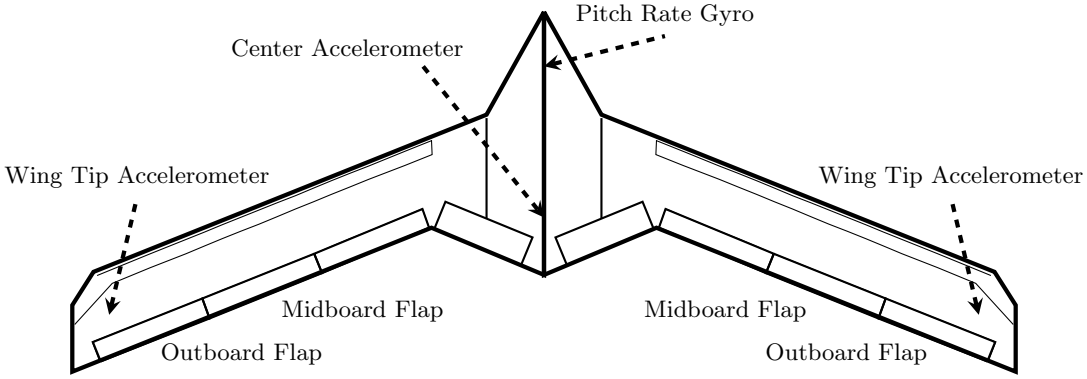

Figure 2. Schematic of the mini MUTT aircraft.

B. Time Delay and Phase Loss Modeling

The goal of this subsection is to describe and model all known parasitic dynamics. For regular flight control systems, the sampling rate is much higher than the closed-loop bandwidth and the induced phase loss from sensors and actuators is usually negligible. On the contrary, active suppression of the flutter instability at high frequency requires a very high closed-loop bandwidth. Actuator and sensor dynamics are not negligible

in this frequency regime. Time delay, introduced by digitalization effects and computation, also has a big impact on the control loop. The question of whether the design should be carried out in discrete time rather than continuous time naturally arises in this context. A discrete time design based on "exact discretization" would automatically incorporate the delay due to the zero-order hold operation. This delay would, however, only be a small part of the overall delay. The remaining part would still require a model. While the advantages of a discrete-time design thus seem to be limited, insight into the problem would be lost to a certain extent. It therefore appears preferable to stay in the continuous-time domain and to include the delay and digitalization effects as part of the model. The controller can be implemented in discrete time by Tustin approximation. Pre-warping can further be used to enhance accuracy in the critical frequency range.

Figure 3 shows all components in the feedback loop and how they are grouped into three models G_{sens}, G_{delay}, and G_{act}. Including these dynamics in the synthesis model allows the controller to compensate for known phase loss and hence to improve performance and robustness. The pitch rate measurement on the mini MUTT aircraft is obtained by an inertial measurement unit (IMU) that includes a 50 Hz low-pass filter. The accelerometer signals are filtered by an analog first order low-pass with a bandwidth of 35 Hz. These components are modeled by two transfer functions

$$G_{\text{accel}}(s) = \frac{2\,\pi\,35}{s + 2\,\pi\,35} \qquad \text{and} \qquad G_{\text{IMU}}(s) = \frac{2\,\pi\,50}{s + 2\,\pi\,50}\,. \tag{2}$$

The signals provided by the sensors are processed by the mini MUTT's flight computer that executes the control algorithm within a 6.6 ms frame. The controller output is passed on to a microcontroller that runs asynchronous with a 3.3 ms frame rate to generate a pulse width modulation (PWM) signal. This PWM signal is the input to a servo controller that runs, also asynchronous, with a 3.3 ms frame. This results in 13.2 ms total computational delay. The actuator used on the mini MUTT is a Futaba S9254 servo. Its physical inertia introduces additional low-pass characteristics. A second-order model

$$G_{\text{act}}(s) = \frac{96710}{s^2 + 840\,s + 96710} \tag{3}$$

is constructed via frequency-domain identification techniques using a chirp input signal. Validation is performed in the frequency domain using a second set of data with an input chirp at a higher voltage and in the time domain via step response data.

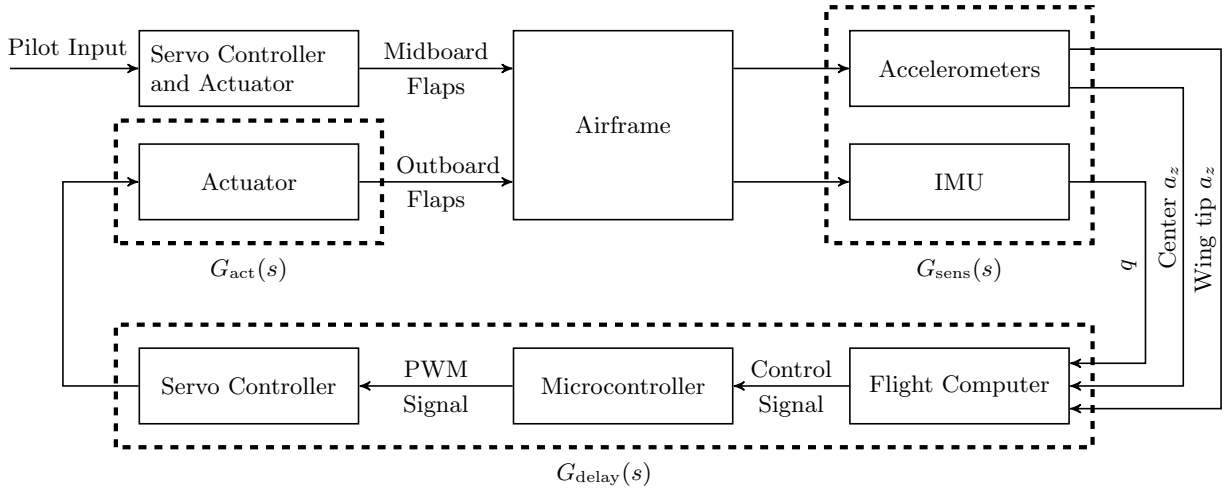

Figure 3. Modeling of components involved in the feedback loop for flutter suppression on the mini MUTT.

In $\mathcal{H}_\infty$ control, every state in the synthesis model directly results in a controller state. To keep the controller order low, it is necessary to combine actuator dynamics, sensor dynamics, and the delay in a low-order equivalent model. Obtaining this model requires a shift of the sensor dynamics from the plant output to the input, which is only possible if all sensors are modeled identically. The slower dynamics of the accelerometers are therefore also assumed for the faster IMU and both are uniformly modeled as $G_{\text{sens}}(s) = G_{\text{accel}}(s)$. Further, all computational frames are added up and a factor of 1.5 is included in order to anticipate the zero-order hold delay. To further account for actuator and sensor delays, a total delay of

25 ms is assumed and modeled as $G_{\text{delay}}(s) = \mathrm{e}^{-0.025\,s}$. A second-order model is calculated from balancing and residualization[22] of $G_{\text{act}}(s)\,G_{\text{delay}}(s)\,G_{\text{sens}}(s)$, where a fifth-order Pade approximation is used for the time delay. The resulting model is

$$G_{\text{equiv}}(s) = \frac{0.966s^2 - 86.33s + 5539}{s^2 + 117.6s + 5539}\,. \tag{4}$$

It captures the phase loss very accurately up to about 100 rad/s, see Figure 4a. Figure 4b further illustrates the phase loss contributions of the known parasitic dynamics in the critical frequency range in detail. The largest contribution comes from the time delay, followed by the actuator and sensors. The resulting simplified loop is depicted in Figure 5. The model G_y is used for the control design and synthesis, described in Section III. It combines the fourth-order airframe model and the second-order equivalent model for actuator dynamics, delay, and sensor dynamics and hence has six states.

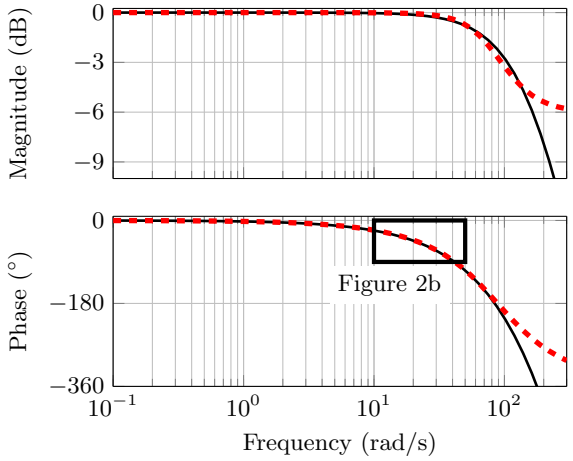

(a) Equivalent phase loss model for inclusion in the synthesis model.

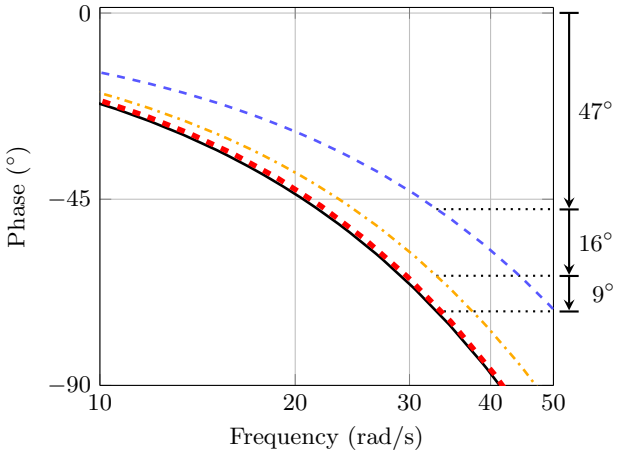

(b) Estimated phase loss at 33 rad/s, the frequency of the aeroelastic mode.

Figure 4. Phase loss due to known parasitic dynamics: pure time delay (- - -), plus actuator dynamics (-·-·-), plus sensor dynamics (——), second-order approximation for synthesis model (▪ ▪ ▪).

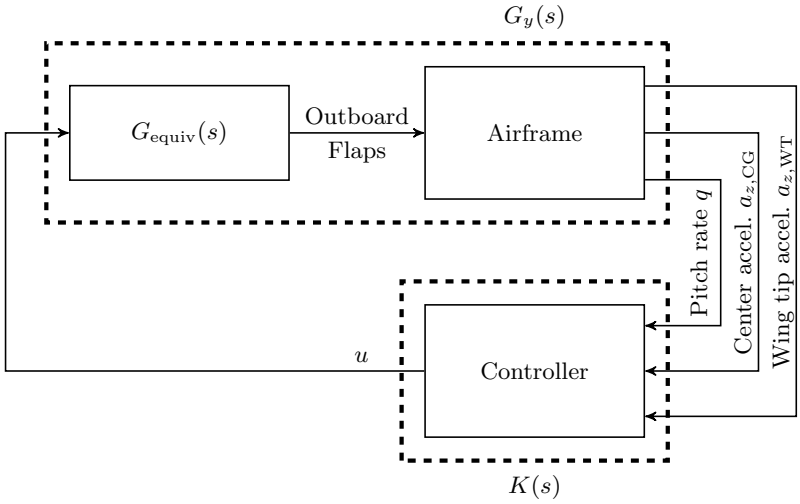

Figure 5. Low-order equivalent modeling of parasitic components involved in the feedback loop.

III. Control Law Design

When flutter was observed at 30 m/s airspeed in a flight test, the aircraft was already running on full throttle. An envelope expansion beyond the flutter speed thus is also limited by the propulsion system.

Noting that the flutter dissipated a certain amount of energy, it appears possible to fly at 33 m/s once the oscillations are controlled. The main objective for the control design is consequently to stabilize flight at 33 m/s and to provide enough safety margin to maintain stability at higher velocities that might occur due to head wind gusts and unintended dive maneuvers. The model described in Section II is thus scaled to an airspeed of $V = 33\,\mathrm{m/s}$, the desired flight point in the expanded envelope. For that flight condition, an $\mathcal{H}_\infty$-norm optimal controller is designed in this section after briefly summarizing the necessary background for $\mathcal{H}_\infty$ control.

A. $\mathcal{H}_\infty$ Closed-Loop Shaping

The $\mathcal{H}_\infty$-norm, or induced $\mathcal{L}_2$-norm, of a linear time invariant (LTI) dynamic system $G(s)$ from input d to output e is defined as

$$\|G(s)\| = \sup_{\omega} \bar{\sigma}(G(\mathrm{j}\omega)) = \sup_{d \in \mathcal{L}_2 \setminus \{0\}} \frac{\|e\|_2}{\|d\|_2}\,, \tag{5}$$

where $\bar{\sigma}(\cdot)$ denotes the largest singular value. This norm measures the maximum gain of the transfer function $G(s)$, i. e., the largest amplification of $\mathcal{L}_2$ input signals over all frequencies and input/output directions. It can be used to specify performance for a feedback interconnection in terms of a generalized plant P. A dynamic controller K can be synthesized by solving two Riccati equations.[23,24] The controller stabilizes the closed-loop interconnection given by the lower fractional transformation $\mathcal{F}_L(P, K)$ and achieves a performance index γ that provides an upper bound on the $\mathcal{H}_\infty$-norm of the closed loop, i. e., $\|\mathcal{F}_L(P, K)\| < \gamma$. With synthesis machinery readily available, e. g., in the Matlab Robust Control Toolbox,[25] the challenging part of any $\mathcal{H}_\infty$ design is to provide meaningful performance specifications.

The high-level objective of the flutter suppression controller is to attenuate the aeroelastic mode without impairing handling of the aircraft by the pilot. The controller further needs to provide robustness against a wide class of possible uncertainties in the model. The proposed generalized plant interconnection, that translates these goals into the objective of minimizing a closed-loop $\mathcal{H}_\infty$-norm, is depicted in Figure 6.

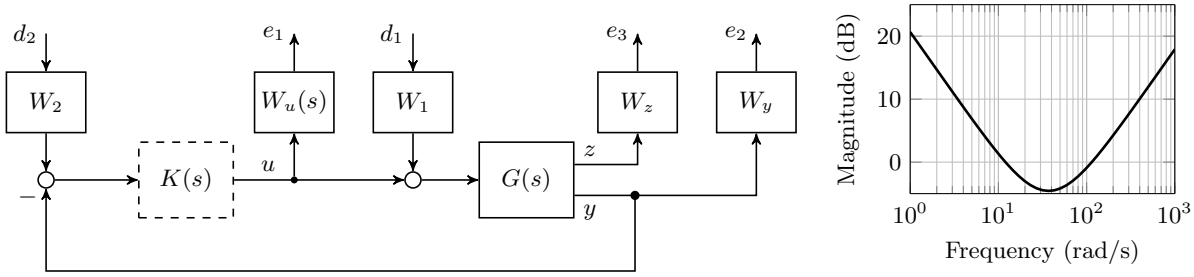

(a) Generalized plant.

(b) Weighting filter $W_u(s)$.

Figure 6. Generalized plant interconnection for the flutter suppression control design.

The plant model is partitioned as $G(s) = \begin{bmatrix} G_z(s) \\ G_y(s) \end{bmatrix}$, where $G_y(s)$ includes the airframe model and the combined actuator dynamics, sensor dynamics, and delay as described in Section II.B. The measurable output y, used for feedback, thus consists of pitch rate (in rad/s), vertical center acceleration, and vertical wing tip acceleration (both in m/s^2). The generalized velocity, $\dot{\eta}_1$, of the first structural mode is added as an additional, non-measurable performance output z to the plant model. This results in a transfer function $G_z(s)$ with a band-pass characteristic and a sharp peak at the flutter frequency. The plant input is the symmetric deflection of the outboard flaps (in rad). Disturbances are modeled both at the plant's input and outputs by exogenous signals d_1 and d_2 that are weighted by W_1 and W_2. The three outputs of the interconnection, e_1 to e_3, are weighted versions of the control signal u, the measurable output y, and the performance output z. These five signals define an input-output map $e = \mathcal{F}_L(P, K)\, d$ that can be represented in terms of six transfer functions as

$$\begin{bmatrix} e_1 \\ e_2 \\ e_3 \end{bmatrix} = \begin{bmatrix} W_u & & \\ & W_y & \\ & & W_z \end{bmatrix} \begin{bmatrix} -T_\mathrm{i} & S_\mathrm{i}\, K \\ G_y\, S_\mathrm{i} & T_\mathrm{o} \\ G_z\, S_\mathrm{i} & G_z\, S_\mathrm{i}\, K \end{bmatrix} \begin{bmatrix} W_1 & \\ & W_2 \end{bmatrix} \begin{bmatrix} d_1 \\ d_2 \end{bmatrix}. \tag{6}$$

The transfer functions $T_\mathrm{o} = G_y\,K\,(I+G_y\,K)^{-1}$ and $T_\mathrm{i} = K\,G_y\,(I+K\,G_y)^{-1}$ are called *output complementary sensitivity* and *input complementary sensitivity*. The transfer function $S_\mathrm{i} = (I + K\,G_y)^{-1}$ is called *input sensitivity*. Further, $S_\mathrm{i}\,K$ and $G_y\,S_\mathrm{i}$ are known as *control sensitivity* and *disturbance sensitivity*. The remaining two transfer functions, $G_z\,S_\mathrm{i}$ and $G_z\,S_\mathrm{i}\,K$, relate the disturbances d_1 and d_2 to the generalized velocity $\dot{\eta}_1$ of the aeroelastic mode. Decreasing their gain thus corresponds to attenuating the aeroelastic mode in response to disturbances.

The desired flutter margin is set by the weight W_z. Larger values result in higher damping augmentation, since the weight encourages the controller to reduce the sharp peak in the frequency response, cf. Refs. 26,27. The weight W_u is used to limit control action to a specific frequency range. The main goal is to avoid undesired interaction with rigid body dynamics in the low-frequency regime and with unmodeled high-frequency dynamics. Selecting W_u as a band-stop filter, as shown in Figure 6b, results in band-pass behavior for both the input complementary sensitivity and the control sensitivity. Thus, both for low and high frequencies $T_\mathrm{i} \approx 0$. The key observation is that this implies $S_\mathrm{i} \approx I$ and consequently $S_\mathrm{i}\,K \approx K$. The band-stop weight W_u thus directly shapes K at low and high frequencies and imposes both a wash-out and a roll-off on the controller. The complementary sensitivities are related to robustness against multiplicative uncertainty at the plant output and input, respectively. When all weights are removed and the loop is closed with a norm-bound, stable LTI dynamic uncertainty $\Delta_1 \in \mathcal{RH}_\infty$ such that $d_1 = \Delta_1\,e_1$, the loop remains stable according to the small-gain theorem[28] as long as $\|\Delta_1\| < 1/\|T_\mathrm{i}\|$. The same is true when the loop is closed with $d_2 = \Delta_2\,e_2$ and $\|\Delta_2\| < 1/\|T\|$. Similarly, the control sensitivity can also be interpreted to guard against an additive uncertainty $d_2 = \Delta_\mathrm{additive}\,e_1$ with $\|\Delta_\mathrm{additive}\| < 1/\|S_\mathrm{i}\,K\|$, and the disturbance sensitivity as to account for inverse uncertainty $d_1 = \Delta_\mathrm{inverse}\,e_2$ with $\|\Delta_\mathrm{inverse}\| < 1/\|G_y\,S_\mathrm{i}\|$. The weights W_y, W_1, and W_2 are used to adjust the relative importance of all involved transfer functions. For more details, the reader is referred to standard robust control textbooks, e. g., Refs. 22, 28.

B. Design and Tuning

The weights for the mixed sensitivity formulation (6) are selected as $W_1 = 1$, $W_2 = \mathrm{diag}(11, 150, 200)$, $W_z = 0.001$, and $W_y = 0.0001\,\mathrm{diag}(3, 3, 6)$. The numbers are the result of tuning but can be seen to essentially normalize all individual transfer functions to a maximum gain of around 0 dB. The weight for the control effort is selected as the interconnection of a low-pass filter with DC-gain 200, crossover frequency 25 rad/s and feedthrough gain 0.5 in series with a high-pass filter with DC-gain 0.5, 55 rad/s crossover frequency and feedthrough gain 200. The resulting band-stop filter $W_u = \frac{100\,s^2+7506\,s+137500}{s^2+12700\,s+1375}$, shown in Figure 6b, thus restricts activity of the flutter suppression controller to the frequency region of the aeroelastic mode. The tuning procedure is simple and intuitive, once initial values are selected to normalize all involved transfer functions. The desired increase in damping, and hence the flutter margin, is set by the weight W_z. To increase robustness margins of the closed-loop (see Section IV.A), $W_u(s)$ is increased in the frequency region where the margin is attained. This consequently decreases the controller gain at that frequency. The relation between input and output margins is handled by the weights W_1 and W_2.

To guide the tuning procedure, Figures 7–9 are used as indicators for nominal controller performance. Figure 7a shows the open-loop and closed-loop transfer function $G_z\,S_\mathrm{i}$ used to specify damping augmentation. The disturbance sensitivity $G_y\,S_\mathrm{i}$ that relates inputs to the measurable outputs is shown in Figure 7b. The sensitivity is in both cases lowered at the frequency of the aeroelastic mode, but as a consequence increased at neighboring frequencies. This is an inevitable consequence of Bode's sensitivity integrals.[22,29] One important

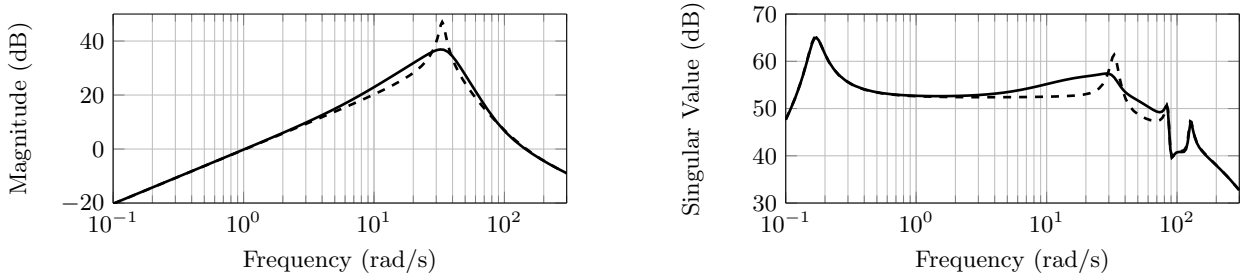

(a) Sensitivity of aeroelastic mode ($G_z\,S_\mathrm{i}$).

(b) Disturbance sensitivity ($G_y\,S_\mathrm{i}$).

Figure 7. Open-loop (- - -) and closed-loop (——) transfer functions.

aspect of the control design is to confine this sensitivity degradation to a specific frequency region. Figure 7 shows that this is indeed achieved and that neither the low frequency phugoid nor the high frequency elastic modes are affected by the flutter suppression controller.

In order to further assess the interaction with pilot commands, a comparison of open-loop and closed-loop step responses to midboard flap deflection is shown in Figure 8 for two different airspeeds. These flaps are used by the pilot to control the longitudinal motion of the aircraft, see Figure 3. The pilot essentially closes a pitch angle feedback loop, since his main visual indicator for control is the vehicles attitude. Maintaining a pitch response as close as possible to the open-loop aircraft is thus considered desirable. The pitch response for the low airspeed of 24 m/s is barely altered by the presence of the flutter suppression controller, see Figure 8. At the naturally unstable airspeed of 33 m/s, the highly oscillatory and divergent pitch rate response is effectively damped out and stabilized. This is achieved without affecting the initial transients up to about 0.15 s. The aircraft's immediate response to pilot inputs is thus identical with and without flutter suppression, both for low and high airspeeds. The flutter suppression controller introduces no additional delay or phase lag, that could impair handling. The effectiveness of the controller is further visible in the acceleration responses in Figure 8b.

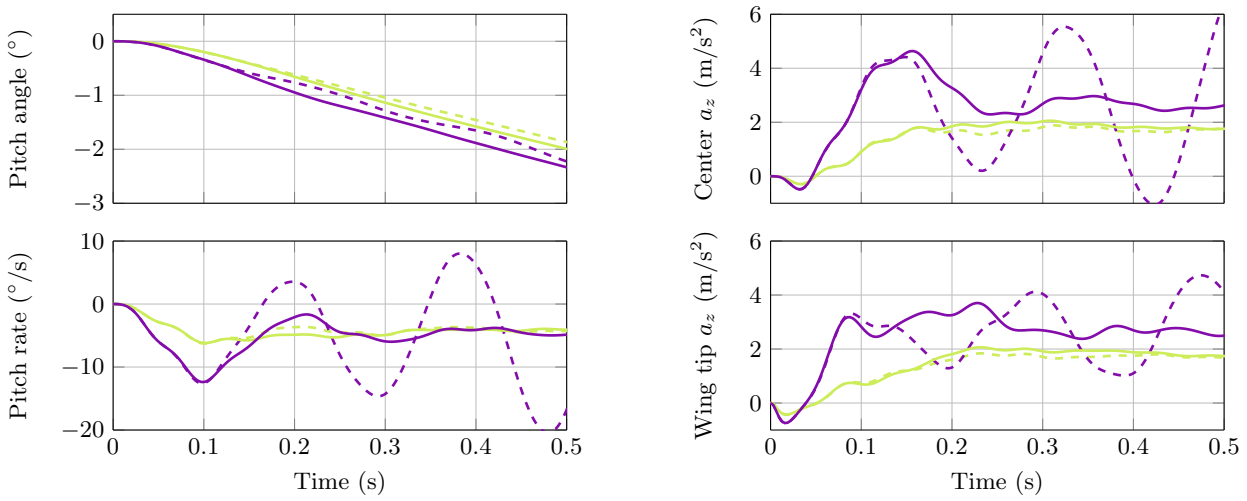

(a) Pitch response.

(b) Acceleration response.

Figure 8. Open-loop responses at 24 m/s (- - -) and 33 m/s (- - -), and closed-loop responses at 24 m/s (——) and 33 m/s (——) to step input at midboard flaps.

The effect of the flutter suppression controller on the pole locations is shown in Figure 9. The open-loop model exhibits flutter at airspeeds above 30 m/s, indicated by the poles of the aeroelastic mode crossing into the right half plane at about 33 rad/s in Figure 9a. Figure 9b shows that the locus of the aeroelastic mode is altered by the controller to stay within the left half plane with a drastic improvement in damping. Extrapolation of the model to higher airspeeds further shows that flutter now occurs at 40 m/s. This corresponds to an envelope expansion of 10 m/s (33 %) and is deemed a more than sufficient safety margin for the desired flight point at 33 m/s. A noticeable side effect of the flutter suppression controller is related to the short period poles. While their damping ratio is only marginally affected, their frequency is lowered for airspeeds below the design point and increased for airspeeds above the design point. Judging from the time-domain responses in Figure 8, the effect is not expected to cause handling quality degradation. With no significant effect on short period damping and the pilot controlling the aircraft almost entirely through its phugoid mode, the effect is of no concern.

The resulting controller $K(s)$ is shown in Figure 10. The desired band-pass behavior is apparent. The controller has eight states. Its fastest pole is at 106 rad/s and thus well within the permissible region for digital implementation on the flight computer. The peak gain for both center acceleration and wing tip acceleration signals is attained at the same frequency around 40 rad/s, but their phase differs considerably. The wing tip acceleration lags the center acceleration by up to 40°. This shows that the proposed controller would be impossible to obtain by a simple combination of the acceleration signals in a single loop.

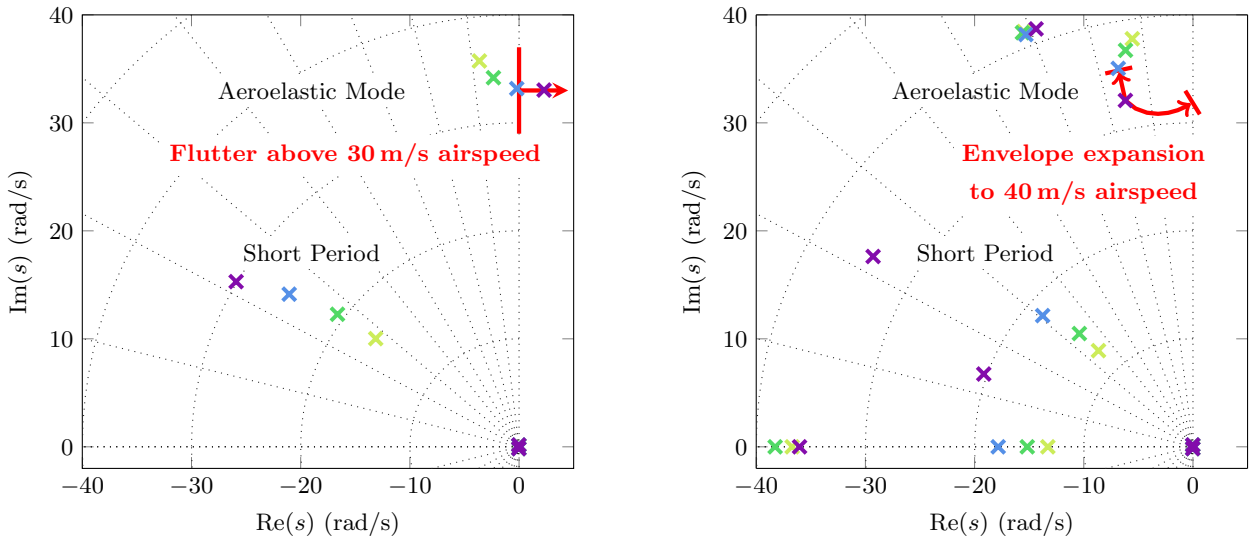

(a) Open-loop pole locations at 24 m/s (×), 27 m/s (×), 30 m/s (×), and 33 m/s (×).

(b) Closed-loop pole locations at 24 m/s (×), 27 m/s (×), 30 m/s (×), and 33 m/s (×).

Figure 9. Effect of the flutter suppression controller on pole locations.

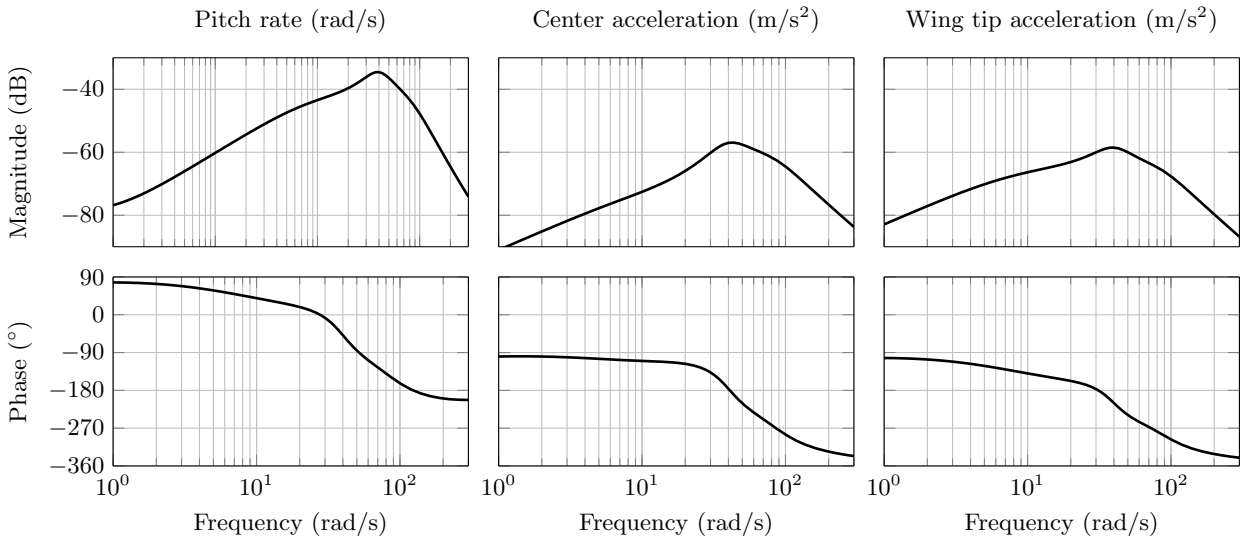

Figure 10. Bode plot of the flutter suppression controller.

IV. Controller Robustness Evaluation

Given the catastrophic consequences of flutter, it is paramount that the controller is highly robust. Without a high-fidelity nonlinear model for evaluation and with limited possibilities for testing outside of the critical flight regime, a thorough linear analysis is required. The robustness tests described in this section aim at maximizing the likelihood of a successful flight with the developed controller. Disk margins, both for single and multivariable loops, are considered. These margins measure robustness with respect to simultaneous phase and gain variations and hence avoid the pitfalls of classical gain and phase margins. Further, structured singular values are used to evaluate robustness with respect to parametric uncertainties in the aircraft model. Specifically, uncertainty in the structural model, the aerodynamics model, and the actuator model is considered. All robustness calculations are performed on a model that includes sensor dynamics, actuator dynamics, delay, the first three structural modes and complete rigid body dynamics. The analysis results of this section are thus to be understood "on top" of all known parasitic dynamics.

A. Robustness Margins

The most common metric to quantify robustness for a control system is given by the classical gain and phase margins. The former specifies how much gain variation a single loop-transfer function can tolerate before instability occurs. The second measures the amount of phase loss that this loop can tolerate. Both margins are independent of each other and common practice in aerospace usually requires at least 6 dB gain margin and 45° phase margin. These numbers are, however, derived from experience with rigid aircraft and certain highly structured control architectures. They are thus not necessarily sufficient for the problem at hand. The flutter suppression controller in Ref. 7, for instance, was designed with 60° phase margins, while the design in Ref. 8 only required 30°. Considering only classical margins can also easily overlook destabilizing combinations of gain and phase that independently are considered safe. It is therefore important to take into account simultaneous gain and phase variations. The corresponding metric is known as *disk margin* and can be calculated from $\|S_\mathrm{o} - T_\mathrm{o}\|$ and $\|S_\mathrm{i} - T_\mathrm{i}\|$.[30] Disk margins provide a higher level of robustness compared to classical margins. They are also easily extended to the multivariable case, allowing for simultaneous perturbation of several loops. A *single-loop input-output disk margin* is obtained by breaking the loop at both the input and at one output at the same time. This margin considers simultaneous perturbations at the input and output of a single feedback loop, with all other loops closed. It is regarded as useful for the present design because independent sensor uncertainties for every channel appear overly conservative, given the same sensor type and data acquisition system for the accelerometers. A simultaneous input and output uncertainty, on the other hand, is inevitably present.

The design requirements are selected as minimum single-loop disk margins of at least 8 dB (45°) and minimum single-loop input/output disk margins of at least 6 dB (37°). These requirements are indicated in Figure 11 as horizontal lines. Further, a minimum single-loop delay margin of 19.8 ms is required, corresponding to one dropped frame from every computational unit and the induced zero-order hold delay. The robustness margins are depicted in Figure 11 as a function of airspeed. All margins uniformly increase with lower airspeed to a similar extent. This indicates a smooth variation without any particular robustness bottlenecks. The input disk margin is above 8 dB (45°) and single-loop output disk margins are all well above 11 dB (60°). The single-loop input/output disk margins also satisfy the requirement of 6 dB (37°). The *multi-loop output disk margin*, corresponding to simultaneous perturbation of all outputs, is also calculated and remains above 6 dB (37°). If independent perturbations of all outputs and the input are considered, the margin is known as *multi-loop input/output disk margin*. It remains above 3.5 dB (23°), which is considered an acceptable level of degradation with respect to the single-loop margins. The delay margins at the outputs are infinite for airspeeds below 33 m/s and the lowest margin is 47 ms at 33 m/s. The lowest delay margin at the input is 22 ms and also attained for 33 m/s.

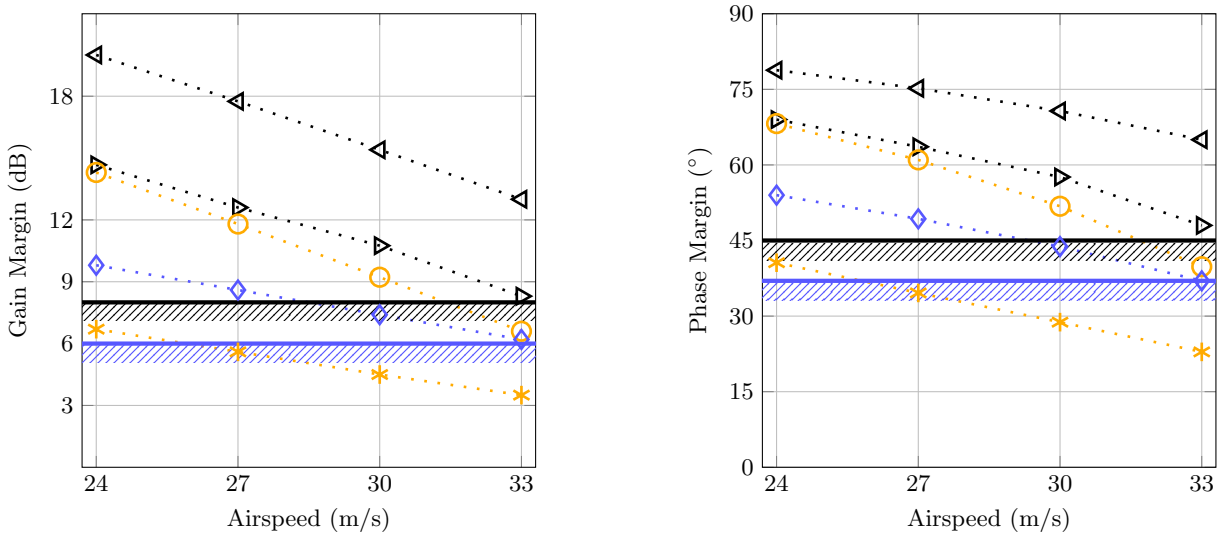

Figure 11. Minimum robustness margins as a function of airspeed: single-loop disk margin at input (· ▷ ·) and output (· ◁ ·), single-loop input-output disk margin (· ◇ ·), multi-loop output disk margin (· ○ ·), and multi-loop input-output disk margin (· ✱ ·).

B. Structured Singular Value Analysis

The margin analysis of Section IV.A aimed at capturing generic model uncertainty. In this subsection, the analysis is narrowed to specific sources of uncertainty within the model structure. The models for both structural dynamics and aerodynamics are best described as uncertain with respect to real parameters. Structured singular value analysis provides an efficient way to calculate stability margins for such structured uncertainties, see Refs. 31, 32. Three different sets of uncertainties are considered in this subsection. *Structural model uncertainty* in the following refers to a real parametric uncertainty in the eigenfrequency ω_1 of the first structural mode. The parameter ω_1 in Eq. (1) is hence replaced by $(1 + \Delta)\,\omega_1$, where $\Delta \in \mathbb{R}$ with nominal value zero spans the range of possible variation, e. g., $|\Delta| < 0.1$ for 10 % uncertainty. Likewise, *aerodynamic uncertainty* refers to real perturbations in the aerodynamic coefficients for pitch moment (M_α, M_q), lift (Z_α, Z_q), and influence of the first structural mode ($\Xi_{1\alpha}$, Ξ_{1q}, $\Xi_{1\delta_2}$) in Eq. (1). All real parametric uncertainties are "complexified" with a 5 % dynamic uncertainty to regularize the resulting computational problem, see Refs. 25, 33 for details. *Actuator uncertainty* refers to a norm-bound complex multiplicative uncertainty in the actuator model, i. e., G_{act} is replaced by $(1 + \Delta)\,G_{\text{act}}$, where $\Delta \in \mathcal{RH}_\infty$ is a norm-bound, stable LTI dynamic uncertainty with nominal value zero that represents the range of variation, e. g., $\|\Delta\| < 0.1$ for 10 % uncertainty. Figure 12a shows the stability boundaries for parameter variations along with a robust performance analysis. The performance index is calculated as the ratio $\|G_z\,S_{\text{i}}\|/\|G_z\|$ of the worst-case $\mathcal{H}_\infty$-norm. It thus measures the amount of damping augmentation that is provided by the flutter suppression controller.

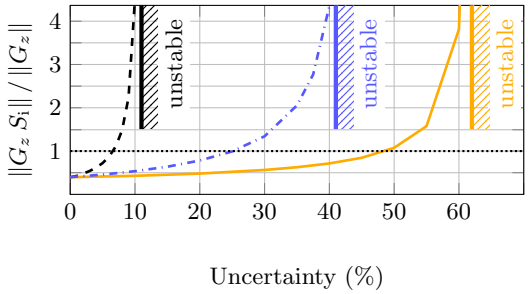

(a) Robust performance analysis for three sets of structured uncertainties.

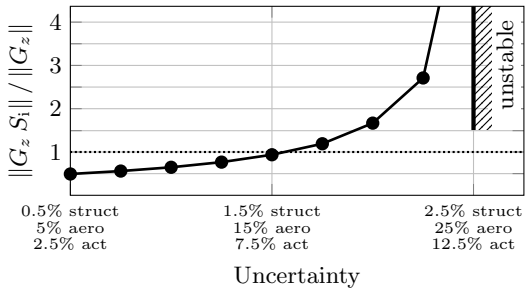

(b) Robust performance analysis with a large uncertainty set.

Figure 12. Robust stability and performance analysis for parametric uncertainties in the structural model (- - -), aerodynamic model (-·-·-), actuator model (——), and a combination of these (—●—).

Instability occurs first for uncertainty in the structural mode frequency. This frequency is obtained from ground vibration tests for the present model in Ref. 34 and expected to be known very accurately, up to about 2 %. Thus, the stability margin of over 10 % is more than sufficient. The highest uncertainty is expected in the aerodynamics model. The analysis shows that the controller is highly robust with respect to this uncertainty, tolerating up to 40 % perturbations. The permissible actuator uncertainty is even higher and is above 60 %. The performance degradation for all three cases is qualitatively similar and can be characterized as graceful. Small variations result in small performance degradation, that only start to increase significantly close to the stability boundary. For individual uncertainties below 7 % in the structural model, 25 % in the aerodynamics model, and 48 % in the actuator model, the ratio of closed-loop and open-loop gain is less than one. In these cases, the controller provides additional damping to the aeroelastic mode and hence achieves robust performance. A fourth analysis is shown in Figure 12b for an uncertainty set that combines all aforementioned uncertainties. Even in this case, performance degradation is smooth and graceful. The stability margin is considerably lower than for the individual uncertainties but still encouraging. Stability is certified up to simultaneous 2.5 % structural mode uncertainty, 25 % aerodynamic uncertainty and 12.5 % actuator uncertainty. Robust performance is achieved up to simultaneous 1.5 % structural mode uncertainty, 15 % aerodynamic uncertainty and 7.5 % actuator uncertainty.

C. Rate Limits and Saturation

Since the system is open-loop unstable, saturation and rate limits must be strictly avoided. This is the main reason for keeping the flutter suppression loop and the control surfaces it uses completely separate from pilot inputs. Doing so prevents the pilot from saturating (and hence disabling) the flutter suppression system with

his or her control inputs. Still, the response of the control system alone must be verified to remain inside the allowed boundaries. Usually, nonlinear simulation is used to assess the likelihood of hitting either rate or deflection limits. Since no such model is available for the present aircraft, a singular value analysis of the linear closed-loop model is performed instead. This analysis does not establish any time-domain guarantees, but provides an estimate of the controller response to worst-case inputs. The maximum deflection of the outboard flaps, used by the controller, is $\delta_{\max} = 35°$. Hardware tests further led to an estimate of 400–1200°/s for the rate limits of the actuators. For the following analysis, the more restrictive bound $\dot{\delta}_{\max} = 400\,°/\mathrm{s}$ is used.

The model is shown in Figure 13. The pilot has direct control over the midboard surfaces, with a maximum deflection of 35°. Gusts are assumed to directly alter the angle of attack by up to 5°. Both pilot and gusts are modeled as first order low-pass filters with 5 rad/s bandwidth and a steady-state gain corresponding to their maximum input magnitude. Modeling gusts in accordance with the Dryden spectrum would result in a similar filter with around half the bandwidth and one third of the gain. The employed model thus provides an additional safety margin. The singular values for both the control signal and its rate are depicted in Figure 13b, normalized by their respective limits. The singular values measure the amplification of a worst-case combination of gust and pilot inputs. A singular value of 0 dB represents the maximum permissible deflection and rate, respectively. The deflection can be seen to max out around −15 dB, indicating that less than about 20 % of the available deflection will actually be used by the controller. The rate increases significantly around the frequency of the flutter frequency, but never exceeds −5 dB. This analysis is very conservative because it largely overestimates the influence of gusts and at the same time considers the worst possible combination with pilot inputs. Still, both the deflection and rate limits are satisfied. This indicates that neither should be of concern for the flutter suppression controller.

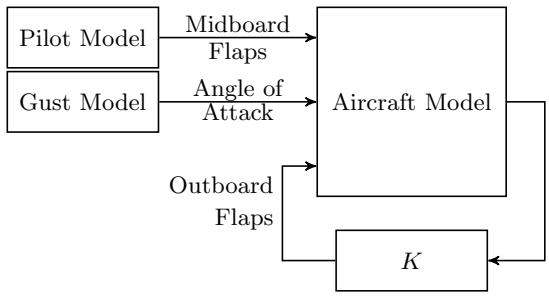

(a) Deflection and rate limit verification model.

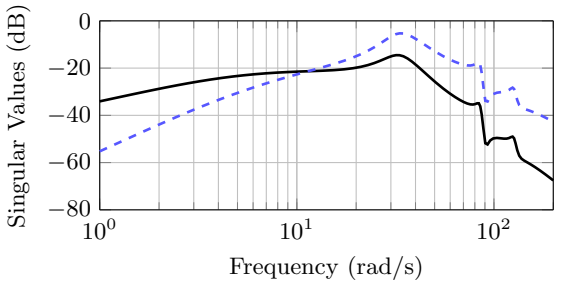

(b) Normalized singular values for deflection ($K\,S_{\mathrm{i}}/\delta_{\max}$ ——) and rate ($s\,K\,S_{\mathrm{i}}/\dot{\delta}_{\max}$ - - -).

Figure 13. Saturation analysis by means of singular values.

V. Conclusions

The present paper developed a systematic multivariable robust control design for a small, unmanned flexible aircraft. The controller requires a large bandwidth in order to stabilize the aircraft. Consequently, all known parasitic dynamics are included in the synthesis model in order to anticipate phase loss. Since the model is highly uncertain, special emphasize is put on a design that is robust with respect to a wide variety of uncertainties. Linear analyses are performed to demonstrate both the high level of robustness and the absence of adverse interaction with low-frequency rigid body dynamics and high-frequency structural dynamics beyond the targeted aeroelastic mode. Validation of the flutter suppression controller in flight tests is planned for the spring of 2016. These flight tests will also provide a comparison to other control approaches and help to establish a benchmark.

Acknowledgement

The authors thank Dale Enns for his insights and helpful discussion. This work was supported by NASA NRA No. NNX14AL36A entitled *Lightweight Adaptive Aeroelastic Wing for Enhanced Performance Across the Flight Envelope*. Mr. John Bosworth is the technical monitor and Mr. Dan Moerder is the acting Technical Monitor.

References

[1]Beranek, J., Nicolai, L., Buonanno, M., Burnett, E., Atkinson, C., Holm-Hansen, B., and Flick, P., "Conceptual Design of a Multi-Utility Aeroelastic Demonstrator," *13th AIAA/ISSMO Multidisciplinary Analysis Optimization Conference*, 2010, pp. 2194–2208.

[2]Ryan, J. J., Bosworth, J. T., Burken, J. J., and Suh, P. M., "Current and Future Research in Active Control of Lightweight, Flexible Structures Using the X-56 Aircraft," *AIAA SciTech*, 2014, doi:10.2514/6.2014-0597.

[3]Preumont, A., *Vibration Control Of Active Structures*, Kluwer Academic Publishers, New York, 2nd ed., 2002.

[4]Wykes, J. H., "Structural Dynamic Stability Augmentation and Gust Alleviation of Flexible Aircraft," *AIAA 5th Annual Meeting and Technical Display*, 1968.

[5]Wykes, J. H., Borland, C. J., Klepl, M. J., and MacMiller, C. J., "Design and Development of a Strutural Mode Control System," Contractor Report 143846, NASA, 1977.

[6]Wykes, J. H., Byar, T. R., MaeMiller, C. J., and Greek, D. C., "Analyses and Tests of the B-1 Aircraft Structural Mode Control System," Contractor Report 144887, NASA, 1980.

[7]Roger, K. L., Hodges, G. E., and Felt, L., "Active Flutter Suppression—A Flight Test Demonstration," *Journal of Aircraft*, Vol. 12, No. 6, 1975, pp. 551–556.

[8]Adams, W. M., Christhilf, D. M., Waszak, M. R., Mukhopadhyay, V., and Srinathkumar, S., "Design, Test, and Evaluation of Three Active Flutter Suppression Controllers," Technical Memorandum 4338, NASA, 1992.

[9]Waszak, M. R. and Srinathkumar, S., "Flutter Suppression for the Active Flexible Wing: A Classical Design," *Journal of Aircraft*, Vol. 32, No. 1, 1995, pp. 61–67.

[10]Mukhopadhyay, V., "Flutter Suppression Control Law Design And Testing For The Active Flexible Wing," *Journal of Aircraft*, Vol. 32, No. 1, 1995, pp. 45–51.

[11]Mukhopadhyay, V., "Transonic Flutter Suppression Control Law Design and Wind-Tunnel Test Results," *Journal of Guidance, Control, and Dynamics*, Vol. 23, No. 5, 2000, pp. 930–937.

[12]Holm-Hansen, B., Atkinson, C., Benarek, J., Burnett, E., Nicolai, L., and Youssef, H., "Envelope Expansion of a Flexible Flying Wing by Active Flutter Suppression," *Proceedings of the Association for Unmanned Vehicle Systems International*, 2010.

[13]Hjartarson, A., Seiler, P. J., and Balas, G. J., "LPV Aeroservoelastic Control using the LPVTools Toolbox," *AIAA Atmospheric Flight Mechanics Conference*, 2013, doi:10.2514/6.2013-4742.

[14]Barker, J. M., Balas, G. J., and Blue, P. A., "Gain-scheduled Linear Fractional Control for Active Flutter Suppression," *Journal of Guidance, Control, and Dynamics*, Vol. 22, No. 4, 1999, pp. 507–512.

[15]Barker, J. M. and Balas, G. J., "Comparing Linear Parameter-Varying Gain-Scheduled Control Techniques For Active Flutter Suppression," *Journal of Guidance, Control, and Dynamics*, Vol. 23, No. 5, 2000, pp. 948–955.

[16]Waszak, M. R., "Robust Multivariable Flutter Suppression for Benchmark Active Control Technology Wind-Tunnel Model," *Journal of Guidance, Control, and Dynamics*, Vol. 24, No. 1, 2001.

[17]Danowsky, B. P., Thompson, P. M., Lee, D., and Brenner, M., "Modal Isolation and Damping for Adaptive Aeroservoelastic Suppression," *AIAA Atmospheric Flight Mechanics Conference*, 2013, doi:10.2514/6.2013-4743.

[18]Schmidt, D. K., "Stability Augmentation And Active Flutter Suppression Of A Flexible Flying-Wing Drone," *submitted to Journal of Guidance, Control, and Dynamics*, 2015.

[19]Pfifer, H. and Danowsky, B., "System Identification of a Small Flexible Aircraft," *AIAA SciTech*, 2016.

[20]Schmidt, D. K., Zhao, W., and Kapania, R. K., "Flight-Dynamics and Flutter Modeling and Analysis of a Flexible Flying-Wing Drone," *AIAA SciTech*, 2016.

[21]Waszak, M. R. and Schmidt, D. K., "Flight dynamics of aeroelastic vehicles," *Journal of Aircraft*, Vol. 25, No. 6, 1988, pp. 563–571.

[22]Skogestad, S. and Postlethwaite, I., *Multivariable Feedback Control*, Prentice Hall, Upper Saddle River, NJ, 2nd ed., 2005.

[23]Glover, K. and Doyle, J. C., "State-space Formulae for All Stabilizing Controllers that Satisfy an $\mathcal{H}_\infty$-norm Bound and Relations to Risk Sensitivity," *Systems & Control Letters*, Vol. 11, No. 3, 1988, pp. 167–172.

[24]Doyle, J. C., Glover, K., Khargonekar, P. P., and Francis, B. A., "State-space Solutions to Standard $\mathcal{H}_2$ and $\mathcal{H}_\infty$ Control Problems," *IEEE Transactions on Automatic Control*, Vol. 34,8, 1989, pp. 831–847.

[25]Balas, G., Chiang, R., Packard, A., and Safonov, M., *Robust Control Toolbox User's Guide R2014b*, MathWorks, 2014.

[26]Hanel, M., *Robust Integrated Flight and Aeroelastic Control System Design for a Large Transport Aircraft*, Ph.D. thesis, University Stuttgart, Stuttgart, Germany, 2001.

[27]Theis, J., Pfifer, H., Balas, G., and Werner, H., "Integrated Flight Control Design for a Large Flexible Aircraft," *American Control Conference*, 2015, pp. 3830–3835, doi:10.1109/ACC.2015.7171927.

[28]Zhou, K., Doyle, J. C., and Glover, K., *Robust and Optimal Control*, Prentice Hall, Upper Saddle River, NJ, 1995.

[29]Stein, G., "Respect the Unstable," *IEEE Control Systems Magazine*, August 2003, pp. 12–25.

[30]Blight, J. D., Lane Dailey, R., and Gangsaas, D., "Practical control law design for aircraft using multivariable techniques," *International Journal of Control*, Vol. 59, No. 1, 1994, pp. 93–137.

[31]Doyle, J., "Analysis of Feedback Systems with Structured Uncertainties," *IEE Proceedings D (Control Theory and Applications)*, Vol. 129, IET, 1982, pp. 242–250.

[32]Packard, A. and Doyle, J., "The Complex Structured Singular Value," *Automatica*, Vol. 29, No. 1, 1993, pp. 71–109.

[33]Packard, A. and Pandey, P., "Continuity Properties of the Real/Complex Structured Singular Value," *IEEE Transactions on Automatic Control*, Vol. 38, No. 3, 1993, pp. 415–428.

[34]Gupta, A. and Seiler, P., "Ground Vibration Test on Flexible Flying Wing Aircraft," *AIAA SciTech*, 2016.